FISEVIER

Contents lists available at ScienceDirect

Journal of Hydrology: Regional Studies

journal homepage: www.elsevier.com/locate/ejrh



Characterizing the spatial-temporal patterns of precipitation in the Qilian Mountains, northwestern China over the past four decades

Xuejia Wang a,b,* o, Kun Wang a, Jiayu Wang a, Yue Yuan a, Guojin Pang c, Xiaohua Gou a,b, Yijia Li a, Qi Wang a, Lanya Liu a, Baktybek Duisebek d, Yermekov Farabi Kerimbayevich e, Meixue Yang f

ARTICLE INFO

Keywords: Qilian Mountains Precipitation variability Elevation dependency Precipitation product In-situ observations

ABSTRACT

Study region: Qilian Mountains (QM), northwestern China.

Study focus: Existing research is constrained by two major limitations: the sparse distribution of meteorological stations introduces uncertainties in spatial interpolation and fails to resolve vertical precipitation structures, particularly the maximum precipitation zone in climate-sensitive regions. This study provides a comprehensive analysis of the spatiotemporal patterns of precipitation in the QM during the past decades, with a specific focus on the elevational distribution and the maximum precipitation zone.

New hydrological insight for the region: Our findings show that the China Meteorological Forcing Dataset (CMFD) reliably captures monthly/annual precipitation variations in the QM, despite minor underestimations identified through station-based validation. Spatially, CMFD reveals a pronounced east-west precipitation gradient throughout the QM. The maximum precipitation zone occurs between 3900 and 4000 m, yet exhibits notable regional variation—shifting from 3300 m in the east to 4200 m in the west. Since 1979, annual precipitation has shown a significant upward trend with distinct spatial heterogeneity—accelerated increases in the arid western areas contrast with moderate growth in the humid eastern areas. Furthermore, these trends display a pronounced elevation dependency. Both monthly precipitation and total precipitation are concentrated between May and September, particularly at mid-to-high altitudes (3700–4200 m). Annual precipitation and its trends show no pronounced longitudinal or latitudinal gradients, underscoring the dominant role of topography over geographic coordinates in modulating precipitation patterns.

E-mail address: wangxuejia@lzu.edu.cn (X. Wang).

^a Key Laboratory of Western China's Environmental Systems (Ministry of Education), College of Earth and Environmental Sciences, Lanzhou University, Lanzhou 730000, China

^b Gansu Liancheng Forest Ecosystem Field Observation and Research Station, Lanzhou University, Lanzhou 730333, China

^c Faculty of Geomatics, Lanzhou Jiaotong University, Lanzhou 730070, China

^d Department of Water Resources and Melioration, Kazakh National Agrarian Research University, Almaty 050010, Kazakhstan

^e Scientific and Educational Technology Platform, Kazakh National Agrarian Research University, Almaty 050010, Kazakhstan

^f Key Laboratory of Cryospheric Science and Frozen Soil Engineering, Northwest Institute of Eco-Environment and Resources, Chinese Academy of Sciences, Lanzhou 730000, China

^{*} Corresponding author at: Key Laboratory of Western China's Environmental Systems (Ministry of Education), College of Earth and Environmental Sciences, Lanzhou University, Lanzhou 730000, China.

1. Introduction

As the primary hydrological driver of Earth's surface systems, precipitation regulates critical hydrosphere-atmosphere-biosphere coupling processes. Since the Industrial Revolution, anthropogenic emissions have driven an unprecedented increase in global surface temperatures. The IPCC AR6 reported that from 2011 to 2020, global temperature was 1.1 °C higher compared to the period from 1850 to 1990, making it the warmest decade on record since 1850 (IPCC, 2021). This thermal perturbation exhibits latitudinal amplification, particularly across the mid-latitudes of the Northern Hemisphere, where amplified warming has accelerated hydrological cycle through thermodynamic intensification, resulting in altered precipitation regimes (Chen et al., 2025; Ji et al., 2014; IPCC, 2021; Jiang et al., 2023; Wang et al., 2018a; Yao et al., 2020). This wields profound and far-reaching influences on ecosystem, socioeconomic structure, as well as sustainable development.

The Qilian Mountains (hereinafter referred to as QM) lie at the intersection of northwest China's arid zone, eastern humid areas, and the cold high-altitude Tibetan Plateau. This strategic geographic location makes the QM a key transitional area between the Asian summer monsoon and mid-latitude westerlies, rendering it particularly sensitive to climate variability (Gou et al., 2015; Wang et al., 2018b; Liu et al., 2024). As a critical ecological security barrier in western China, the QM severs as an important water source of the Yellow River and several inland rivers (such as Shiyang River, Heihe River, and Shule River), as well as a priority area of biodiversity conservation (Li et al., 2019; Wang et al., 2019; Zhu et al., 2022). Given these ecological imperatives, a comprehensive understanding of precipitation dynamics is crucial for uncovering regional responses to global climate changes and formulating science-based conservation strategies for water resources management and ecosystem preservation.

Early in 2002, Shi first identified a hydroclimatic regime shift in northwest of China (encompassing the QM), documenting 1987–2002 precipitation increases, accelerated glacier melting, and elevated streamflow. This evidence base supported their pioneering hypothesis of warm-dry to warm-wet transition through coupled cryosphere-hydrosphere response analysis (Shi, 2002; Shi et al., 2003). Subsequent investigations revealed complex spatial heterogeneity in the dry-wet evolution of northwest China (e.g., Long et al., 2018; Zhang et al., 2007, 2021; Deng et al., 2022). Zhang et al. (2007) found opposing Palmer Drought Severity Index trend from 1953 to 2003: a dry-wet-dry pattern in the east and wet-dry-wet in the west. Huang et al. (2011) reported significant humidification across the region during 1960–2009, especially after 1987, using Humid Index. While Long et al. (2018) suggested limited statistical significance in the warm-humid transition during 1948–2010 based on standardized moisture anomaly index. Several studies regionalizing the northwestern China similarly confirm a general wetting trend over the recent 50 years, yet highlight a distinct east-west contrast: drying in the east and wetting in the west (Han et al., 2016; Zhang et al., 2019, 2021). This east-west moisture gradient, superimposed on large-scale warming, underlines the critical importance of mesoscale atmospheric processes and topographic effects in modulating regional climate responses.

Variations in precipitation serve as a key indicator of regional aridity and humidity. Precipitation in the QM exhibits significant spatial variability, generally higher in eastern and mountainous areas than in western or plain regions (Wang et al., 2018b). Several studies reported divergent trends. For instance, Yin et al. (2009) indicated an increasing precipitation from 1956 to 2006, most notably in the west. While Jia et al. (2008) noted an insignificant increase trend from 1960 to 2005, though increases became pronounced after 2000. Cheng et al. (2020) identified significant increase in the central QM between 1961 and 2017. The spatial variability of precipitation in the QM is governed by geographical location, topography, and altitude gradients. Additionally, influenced by global climate change and evolving large-scale circulation patterns, mesoscale convective systems have also undergone notable changes, affecting precipitation variability (Wang et al., 2019; Geng et al., 2017). Altitudinal precipitation patterns vary considerably by mountain areas, latitudes, slopes orientation, seasons, and wet/dry conditions (Wang et al., 2009). Lin (1995) established that mountains below 2600 m exhibit precipitation maxima at peaks, higher mountains display a maximum precipitation belt at mid-altitude, the height of which depends on the climate dry/wet conditions. For the QM specifically, Tang (1985) proposed that precipitation follows an S-curve distribution with altitude, indicating distinct maximum and minimum elevation zones. Zhang et al. (2008) argued that precipitation increases with altitude in this region. Therefore, the spatial variability of precipitation in the QM, particularly the existence and location of the maximum precipitation zone, remains unsolved.

For decades, scientific understanding of the QM's climate patterns has primarily relied on meteorological stations. However, these stations are often sparsely and unevenly distributed, particularly in mountainous areas and low altitudes. As a result, this heterogeneous distribution creates inherent limitations in spatial representativeness of these stations, leading to findings that often do not fully encapsulate the actual spatial-temporal dynamics of precipitation in the QM. While high-resolution satellite data and climate models-simulated data present their own sets of challenges. For instance, satellite data suffer from issues such as insufficient time coverage and low retrieve rates, particularly under persistent cloud cover conditions (Wang et al., 2018a). Climate models, on the other hand, tend to have relatively coarse spatial resolution and are plagued by well-documented biases in climate variables (Chen et al., 2022; Lalande et al., 2021; Li et al., 2025a; Liu et al., 2022; Wang et al., 2021). This study selects a reliable precipitation dataset based on meteorological stations and *in-situ* observations to revisit the spatiotemporal variations in precipitation across the QM. The region is further delineated into sub-regions to examine the elevation-dependent characteristics of precipitation under varying topographic and geographic conditions. The objectives of this study are to characterize the spatiotemporal patterns of precipitation in the QM and to pinpoint the existence and location of a maximum precipitation zone within the region. Our study is expected to enhance the understanding of precipitation variability across the QM, providing a scientific foundation for mountain climate and hydrology simulations, sustainable water resource management, and ecological stability maintenance within the region.

The remainder of this manuscript is organized as follows. Section 2 describes the data sources and method used in this study. Section 3 presents the validation of precipitation products using meteorological station observations. Based on these validations, Section 3 uses the most reliable dataset to investigate the spatial and temporal distribution and variations of precipitation, with

emphasis on precipitation variations across different elevations. Section 4 discusses the principal findings and their implications, along with potential future research directions. Finally, the conclusions of this investigation are summarized in Section 5.

2. Data and method

2.1. Research area and observational data

The Qilian Mountains (QM) is suited in the northeastern Tibetan Plateau (stretching from $93^{\circ}30'E$ to $103^{\circ}E$ and $36^{\circ}30'N$ to $39^{\circ}30'N$), spanning across the provinces of Qinghai and Gansu in China. Situated at the convergence of the Tibetan Plateau, the Loess Plateau, and the Inner Mongolia Plateau, the QMs consists of several parallel mountain ranges and wide valleys, all oriented northwest to southeast. The range starts from Songshan at Wushaoling in the east and to the Dangjin Mountain Pass in the west, with the Heihe River to its north. The QM stretches around 800 km from east to west and 200–400 km from south to north, with elevations ranging from 1600 to 5700 m. This region hosts 2684 glaciers, covering a total area of 1597.81 ± 70.30 km² (Sun et al., 2015). Geomorphologically, the study area features gentle southern slopes contrasting with steep northern slopes. The terrain is generally higher in the west than in the east and higher in the south than in the north. Mountain ranges trend northwest-southeast, with peaks typically between 4000 and 5500 m. The highest peak, located in the Shule south mountain, reaches 5808 m. Peaks exceeding 4000 m maintain year-round snow cover, while intermontane valleys lie at elevations of 3000–3500 m. Modern glaciers are primarily found above 4500–5000 m. Major rivers in the QM include the Datong, Shiyang, Heihe, and Shule Rivers. The primary lakes include Qinghai Lake, Hala Lake, and Sugan Lake (Li et al., 2019). The sustainable development of the Hexi Corridor's oases is fundamentally constrained by water resources from the QM. Influenced by Asian monsoons and mid-latitude westerlies, the climate in the QM features long, dry, cold winters and short, wet, cool summers.

The precipitation data used in this study includes the China Meteorological Forcing Dataset, the long-term high spatial-temporal resolution monthly climate dataset, China 1 km resolution monthly precipitation dataset, and ERA5 reanalysis data. To assess the reliability of these datasets, we selected data from 30 meteorological stations within and around the QM and data from five field observation sites, ensuring comprehensive evaluation of the precipitation products performance across topographic gradients (shown in Fig. 1).

The meteorological station recorded daily precipitation data used in this study is sourced from the "China Surface Climate Daily Data Set (V3.0)" provided by the China Meteorological Data Network (http://data.cma.cn/). This dataset was derived from 699 baseline and basic meteorological stations across China, starting from January 1951. The observed precipitation data underwent quality control by the National Meteorological Information Center for the China Meteorological Administration during its generation. For the suspicious and erroneous data identified, manual verification and correction were generally carried out. To validate the reliability of the gridded data, this study selected data from 30 meteorological stations located within and around the QM. The time

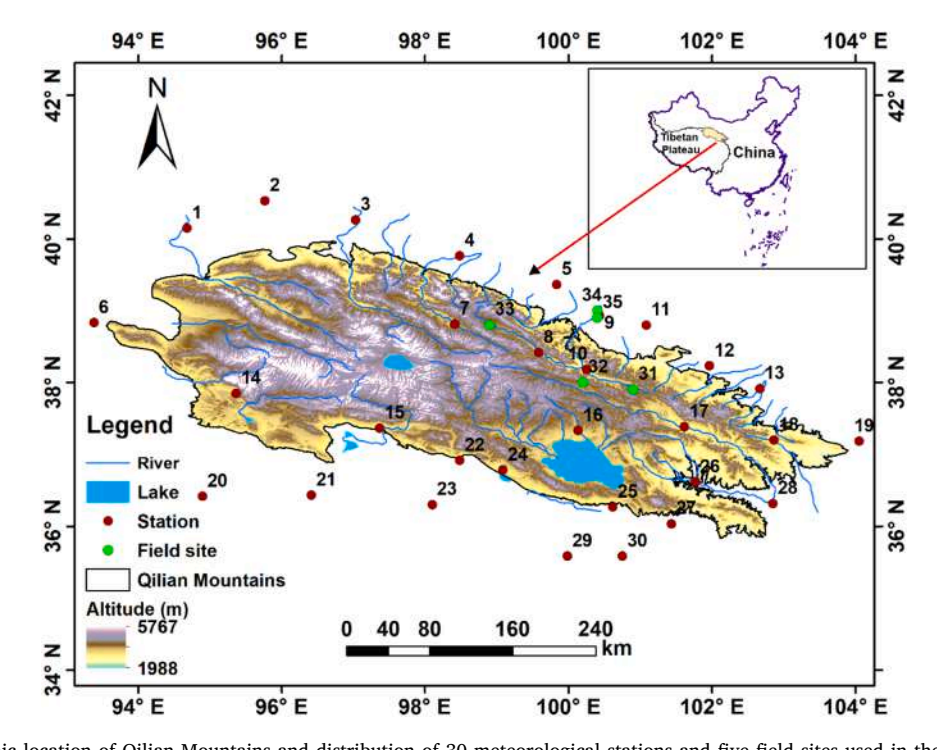


Fig. 1. Geographic location of Qilian Mountains and distribution of 30 meteorological stations and five field sites used in the study. Station information is shown in Table 1.

span of the data is from 1951 to 2017, with detailed station information shown in Table 1. The missing rates for daily precipitation data were generally below 13.4 % at all stations except Wulan station (44.4 %). To avoid introducing interpolation errors, we did not interpolate the daily data due to its discrete nature at both spatial and temporal scales. For the monthly data, however, we performed interpolation using values from neighboring months to ensure data integration and allow for straightforward comparisons.

The raw data for the CMFD is partially sourced directly from primary meteorological sources available on the China Meteorological Data Network, and its precipitation also integrates meteorological observational data to varying degrees. To comprehensively evaluate the CMFD's performance, this study selected monthly precipitation data from five independent field stations (including Ebao recorded in 2014, Yakou in 2018, Dashalong in 2014, Zhangye Wetland in 2013, and Daman in 2014) located at different locations and altitudes in the QM. These validation datasets were sourced from the National Tibetan Plateau Data Center (https://data.tpdc.ac.cn/). Detailed station information is provided in Table 1.

2.2. Reanalysis data

2.2.1. China meteorological forcing dataset (CMFD)

The China Meteorological Forcing Dataset (CMFD) includes seven surface meteorological elements: near-surface temperature, near-surface pressure, near-surface specific humidity, near-surface wind speed, downward shortwave and longwave radiation, and surface precipitation rate (source: https://www.tpdc.ac.cn/zh-hans/data/8028b944-daaa-4511-8769-965612652c49/). The dataset features a temporal resolution of 3 h and a spatial resolution of 0.1°, covering the period from January 1979 to December 2018 (He et al., 2020). This dataset uses existing Princeton reanalysis data, GLDAS data, GEWEX-SRB radiation data, and TRMM precipitation data as background fields, integrating the routine precipitation observation data released by the China Meteorological Administration. The raw data come from meteorological station observations, reanalysis data, and satellite remote sensing data. Non-physical values have been removed, and the ANU-Spline statistical interpolation method was applied to create the dataset. The accuracy of the CMFD data lies between station observation data and satellite remote sensing data, outperforming the precision of existing reanalysis data (Yang et al., 2010; He et al., 2020).

2.2.2. Long-term high-resolution monthly climate dataset (LZU0025)

The long-term high-resolution monthly climate dataset (LZU0025) provides monthly records of temperature and precipitation at a

Table 1 Information of 30 meteorological stations and five field observation sites.

No.	Station ID	Station name	Altitude (m)	Longitude (°)	Latitude (°)
1	52418	Dunhuang	1138.7	94.7	40.1
2	52424	Anxi	1170.8	95.8	40.5
3	52436	Yumenzhen	1526.0	97.0	40.3
4	52533	Jiuquan	1477.2	98.5	39.8
5	52546	Gaotai	1332.2	99.8	39.4
6	52602	Lenghu	2733.0	93.4	38.8
7	52633	Tuole	3360.7	98.4	38.8
8	52645	Yeniugou	3180.0	99.6	38.4
9	52652	Zhangye	1482.7	100.4	38.9
10	52657	Qilian	2787.4	100.3	38.2
11	52661	Shandan	1764.6	101.1	38.8
12	52674	Yongchang	1976.1	102.0	38.2
13	52679	Wuwei	1530.8	102.7	37.9
14	52713	Dachaidan	3173.2	95.4	37.9
15	52737	Delingha	2981.5	97.4	37.4
16	52754	Gangcha	3301.5	100.1	37.3
17	52765	Menyuan	2707.6	101.6	37.4
18	52787	Wushaoling	3045.1	102.9	37.2
19	52797	Jingtai	1630.5	104.1	37.2
20	52818	Geermu	2807.7	94.9	36.4
21	52825	Nuomuhong	2790.4	96.4	36.4
22	52833	Wulan	2950.0	98.5	36.9
23	52836	Dulan	3191.1	98.1	36.3
24	52842	Chaka	3087.6	99.1	36.8
25	52856	Qiabuqia	2835.0	100.6	36.3
26	52866	Xining	2261.2	101.8	36.6
27	52868	Guide	2237.1	101.4	36.0
28	52876	Minhe	1813.9	102.8	36.3
29	52943	Xinghai	3323.2	100.0	35.6
30	52955	Guinan	3200.6	100.8	35.6
31	-	Ebao	3294	100.9	37.9
32	_	Yakou	4148	100.2	38.0
33	-	Dashalong	3729	98.9	38.8
34	-	Zhangye Wetland	1460	100.4	39.0
35	_	Daman	1556	100.4	38.9

high resolution of 0.025°, spanning from January 1951 to December 2011 (https://doi.pangaea.de/10.1594/PANGAEA.895742, Zhao et al., 2019). The LZU0025 dataset is based on data from 1202 precipitation stations across China and its surrounding countries. It uses the local thin-plate spline method through the ANUSPLIN software for interpolation. The quality assessment of the dataset indicated satisfactory simulation abilities. When compared with 265 remaining station observation data, the results showed that from 1951 to 2011, the LZU0025 monthly interpolated data closely matched the observed data, with an average absolute difference of 70.5 mm and a standard deviation of 122.6 mm. The LZU0025 dataset offers researchers detailed historical climate information and can be used as a crucial resource for environmental modeling and regional climate analysis (Zhao et al., 2019).

2.2.3. China 1 km resolution monthly precipitation dataset (CN-1km)

The China 1 km resolution monthly precipitation dataset (CN-1km) has a temporal resolution of 1 month and a spatial resolution of 0.0083333° (approximately 1 km), with a time period spanning from January 1901 to December 2024 (https://www.tpdc.ac.cn/zh-hans/data/faae7605-a0f2-4d18-b28f-5cee413766a2). This dataset was generated for China domain through Delta spatial downscaling techniques, based on the Climatic Research Unit global 0.5° climate dataset and the high-resolution WorldClim global climate dataset. It was validated using data from 496 independent meteorological observation stations, and the validation results are reliable (Peng et al., 2019).

2.2.4. ERA5 reanalysis precipitation dataset (ERA5)

The ERA5 dataset, developed by European Centre for Medium-Range Weather Forecasts, is the fifth-generation atmospheric reanalysis dataset for global climate (Hersbach et al., 2020). It spans from January 1950 to the present and includes climate variables such as 2-meter air temperature and total precipitation, with data available at monthly, daily, and hourly resolutions, and a spatial resolution of 0.25° (https://cds.climate.copernicus.eu/datasets/reanalysis-era5-single-levels-monthly-means?tab=overview). The ERA5 reanalysis uses data assimilation techniques to combine atmospheric model simulations with extensive observational data from around the world, creating a comprehensive and consistent global dataset. Compared to traditional satellite retrievals and numerical model outputs, the ERA5 dataset offers higher spatial and temporal coverage and resolution, making it well suitable for large-scale and long-duration climate studies.

2.2.5. Large-scale climate oscillation index

To discuss the possible drivers of annual precipitation changes in the QM, we conducted correlation analyses between regional annual precipitation and large-scale climate indices, including oceanic-atmospheric circulation indices and monsoon indices. The oceanic-atmospheric indices, including the Pacific Decadal Oscillation (PDO), Atlantic Multidecadal Oscillation (AMO), Arctic Oscillation (AO), and the Multiple ENSO Index (MEI), were obtained from the National Oceanic and Atmospheric Administration of the United States (https://psl.noaa.gov/data/climateindices/). The North Atlantic Oscillation (NAO) index, the South Asian Summer Monsoon Index (SASMI), and the East Asian Summer Monsoon Index (EASMI) were sourced from the website of Prof. Jianping Li (http://lijianping.cn/dct/page/1).

2.3. Precipitation product evaluation method

Compared to station data, precipitation products have greater continuity in both temporal and spatial scales. However, it remains uncertain whether these datasets can accurately reflect the precipitation variation patterns in the QM. Therefore, precipitation data from 30 meteorological stations and the corresponding grid precipitation values from precipitation products were compared using correlation coefficient (COR), bias, mean absolute error (MAE), and root mean square error (RMSE).

(1) Correlation coefficient (COR)

$$COR = \frac{\sum_{i=1}^{N} (x_i - \overline{x})(y_i - \overline{y})}{\sqrt{\sum_{i=1}^{N} (x_i - \overline{x})^2 \sum_{i=1}^{N} (y_i - \overline{y})^2}}$$
(1)

(2) Bias

$$Bias = \overline{y} - \overline{x} \tag{2}$$

(3) Mean absolute error (MAE)

$$\mathbf{MAE} = \frac{1}{N} \sum_{i=1}^{N} |(\mathbf{y}_i - \mathbf{x}_i)|$$
(3)

(4) Root mean square error (RMSE)

$$RMSE = \sqrt{\frac{1}{N} \sum_{i=1}^{N} (y_i - x_i)^2}$$
 (4)

Where x_i is the station observational data; y_i is the grid data; \overline{x} is the mean value of the station observational data; \overline{y} is the mean value of the gridded data; \overline{y} is the sample size.

2.4. Linear trend analysis

To investigate the interannual variation of annual precipitation, a linear trend analysis (Eq. 5) was performed with time as the independent variable. The statistical significance of the trend was assessed using a Student *t*-test.

Trend =
$$\frac{n \sum_{i=1}^{n} (x_{i}y_{i}) - \sum_{i=1}^{n} x_{i} \sum_{i=1}^{n} y_{i}}{n \sum_{i=1}^{n} (x_{i})^{2} - (\sum_{i=1}^{n} x_{i})^{2}}$$
(5)

Here, x_i and y_i denote the time series and annual precipitation, respectively. n denotes the length of study period.

3. Results

3.1. Validation of precipitation products

Four sets of monthly precipitation products were assessed for their accuracy against ground-based meteorological observations (Fig. 2). Among all the products, the CMFD demonstrates the best performance with a linear fitting slope of 0.99 (p < 0.05). Compared

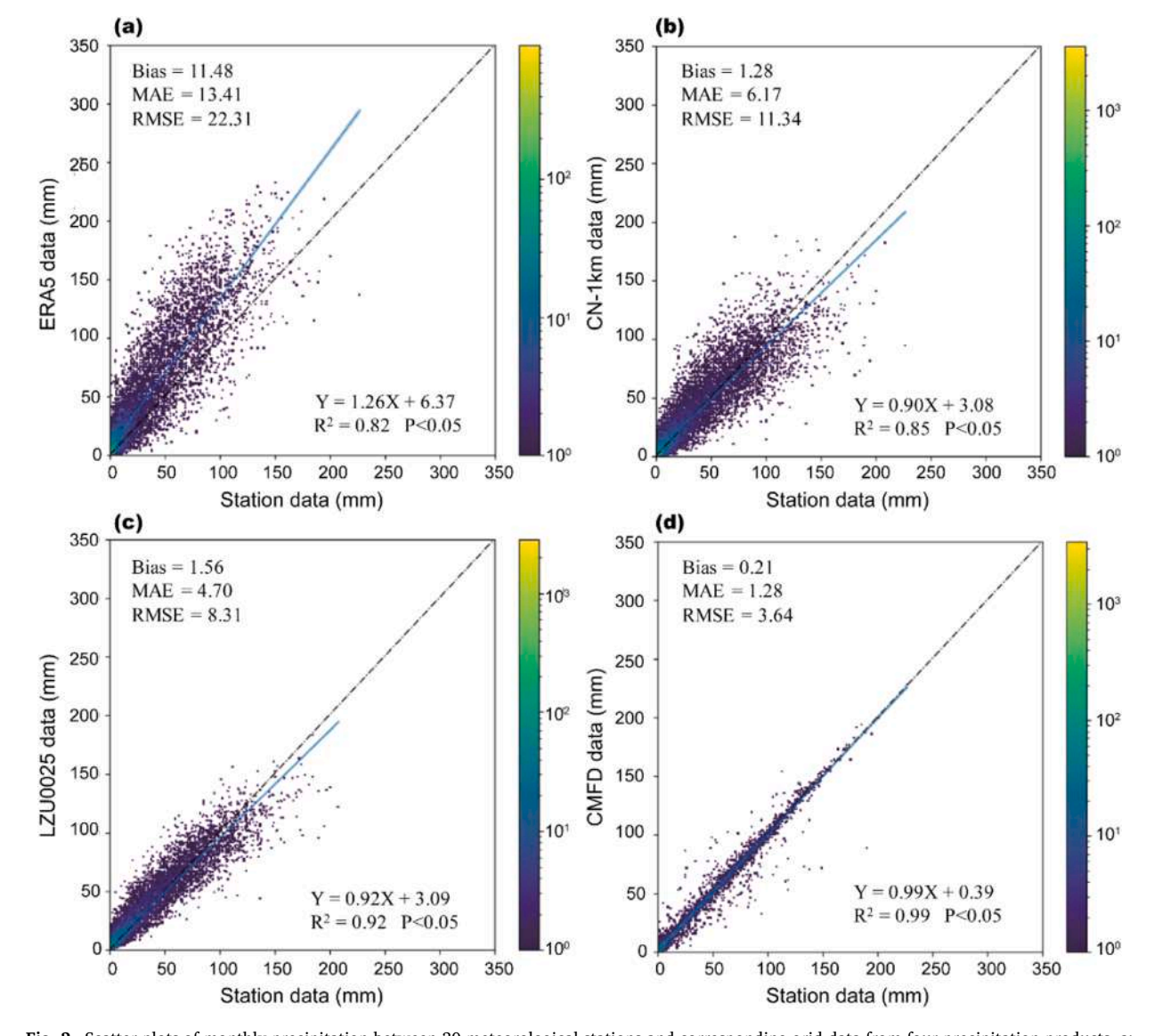


Fig. 2. Scatter plots of monthly precipitation between 30 meteorological stations and corresponding grid data from four precipitation products. a: ERA5 reanalysis data, b: China 1km-resolution monthly precipitation data (CN-1km), c: LZU0025, d: CMFD.

to other products, CMFD exhibits the lowest bias (0.21 mm), RMSE (3.64 mm), and MAE (1.28 mm). These robust statistical indicators confirm CMFD's validity for characterizing precipitation patterns in the QM.

Fig. 3 compares the regional average annual precipitation anomalies from 30 meteorological stations against the corresponding grid data from four reanalysis products, using the maximum temporal coverage available within each dataset. Among the four products, CMFD demonstrates the most favorable performance in both capturing variation trends and minimizing annual precipitation errors, followed by the LZU0025 data. While the LZU0025 can effectively reflect the observed variation trends from station data, it exhibits substantial discrepancies during certain periods, particularly between 1951–1979 when it markedly overestimates precipitation. The CN-1km data also mirrors the variation trends well but suffers from larger overall errors compared to both the CMFD and LZU0025 data. The ERA5 data generally follows the observed variation patterns but shows notable deviations during specific years, particularly since the 1990s, along with relatively high overall errors. We also compared 13 station observations within the QM with station-corresponding CMFD data (Figure S1 in Supplementary material). The results confirmed that while there are local differences, the CMFD reliability replicates annual precipitation, well aligning with the results exhibited in Fig. 3.

To further ensure the reliability of the CMFD data, we conducted additional validation using five independent *in-situ* observations. The correlations of monthly precipitation between station data and the corresponding CMFD grid data are significantly high, with a correlation coefficient R² of 0.99. Meanwhile, the intra-annual variations of monthly precipitation from CMFD are consistent with those of the station data. Although a minor systematic overestimation is observed, the marginal magnitude of this discrepancy (Fig. 4) confirms CMFD's overall reliability for regional hydrometeorological studies. Based on these comprehensive evaluations, CMFD was selected as the primary dataset for subsequent temporal and spatial precipitation analyses in the QM.

3.2. Spatial and temporal distribution of precipitation in the QM

The below, we primarily use CMFD data to characterize spatial patterns and temporal variability of precipitation in the QM. Over the 40-year period from 1979 to 2018, the average annual precipitation in the QM shows an uneven distribution pattern characterized by lower precipitation in the west and higher levels in the east, generally exhibiting a decreasing trend from east to west (Fig. 5). The 400 mm isohyet approximately divides the QM into two distinct regions: the western area being semi-arid and most of the eastern area semi-humid. Across the whole QM, the maximum annual precipitation reaches 550 mm near Mengyuan station, while the minimum precipitation of 28 mm is observed around Lenghu station. Two distinct precipitation centers are observed in the eastern mountainous areas, both receiving approximately 500 mm of annual precipitation. In the western low-altitudes of the QM, average annual precipitation remains below 200 mm, whereas eastern low-altitudes receives around 300 mm, with precipitation decreasing with increasing altitude.

The average seasonal precipitation in the QM (excluding winter) exhibits a distribution pattern consistent with the average annual precipitation, generally showing a decreasing trend from east to west (Fig. 5). Precipitation during winter, spring, and autumn remains relatively low, with summer precipitation accounting for half of the annual total. The average seasonal precipitation in the eastern area is significantly higher than in the west. In summer, the entire western area receives less than 200 mm of precipitation, while two distinct precipitation centers are observed in the eastern area. There are two smaller precipitation centers in the western area exceeding 100 mm and 150 mm respectively, corresponding to the high-altitude areas in the western QM. The spatial patterns of spring and autumn precipitation in the QM are highly similar, though spring receives slightly more precipitation than autumn. Isohyet analysis reveals that the contour lines of equal precipitation extend farther east in spring compared to the autumn distribution. In winter, no discernible precipitation center is observed.

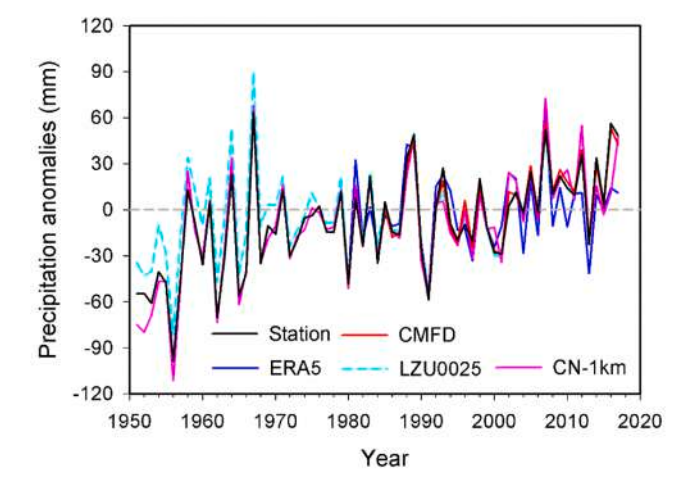


Fig. 3. Annual precipitation anomalies in the Qilian Mountains from 1951 to 2017, derived from 30 meteorological stations and the corresponding grid data of four precipitation products. The climatological mean of the 1981–2010 period is used as the reference. The evaluation period for each reanalysis product against observations is dictated by the availability of the validation data.

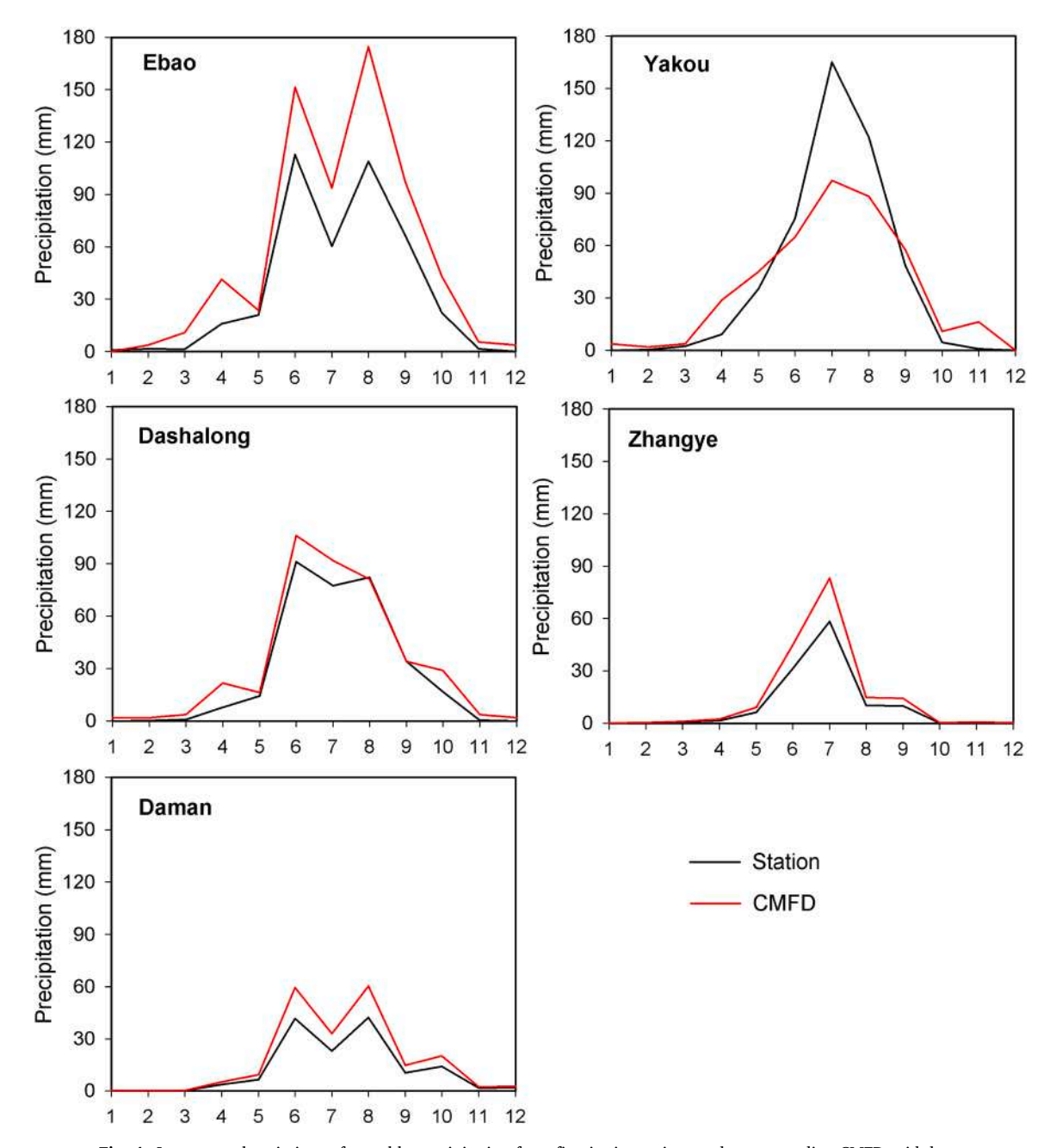


Fig. 4. Intra-annual variations of monthly precipitation from five in-situ stations and corresponding CMFD grid data.

3.3. Precipitation variation with elevation, latitude, and longitude

The spatial distribution of precipitation is closely related to geographical factors such as longitude, latitude, and elevation. In this section, we analyzed both average annual precipitation and total annual precipitation—the latter defined as the product of annual precipitation and area—across various elevation gradients and geographical coordinates. Multiplying annual precipitation by area yields the total annual precipitation, a measure that converts a simple precipitation amount into the actual volumetric water input. Since precipitation is rarely uniform across topographically complex regions, using a simple average—which weights all measurement points equally, regardless of the spatial area they represent—fails to capture the total volume of water received by the region. The total annual precipitation, however, provides a physically meaningful quantity of the actual water volume supplied to a given region or zone.

Within the QM delineated in this study, the elevation ranges from 2200 to 5000 m, with geographical coordinates spanning 35.8°N-40.0°N and 93.5°E-104.0°E. The analyses of average annual precipitation and total annual precipitation were performed using

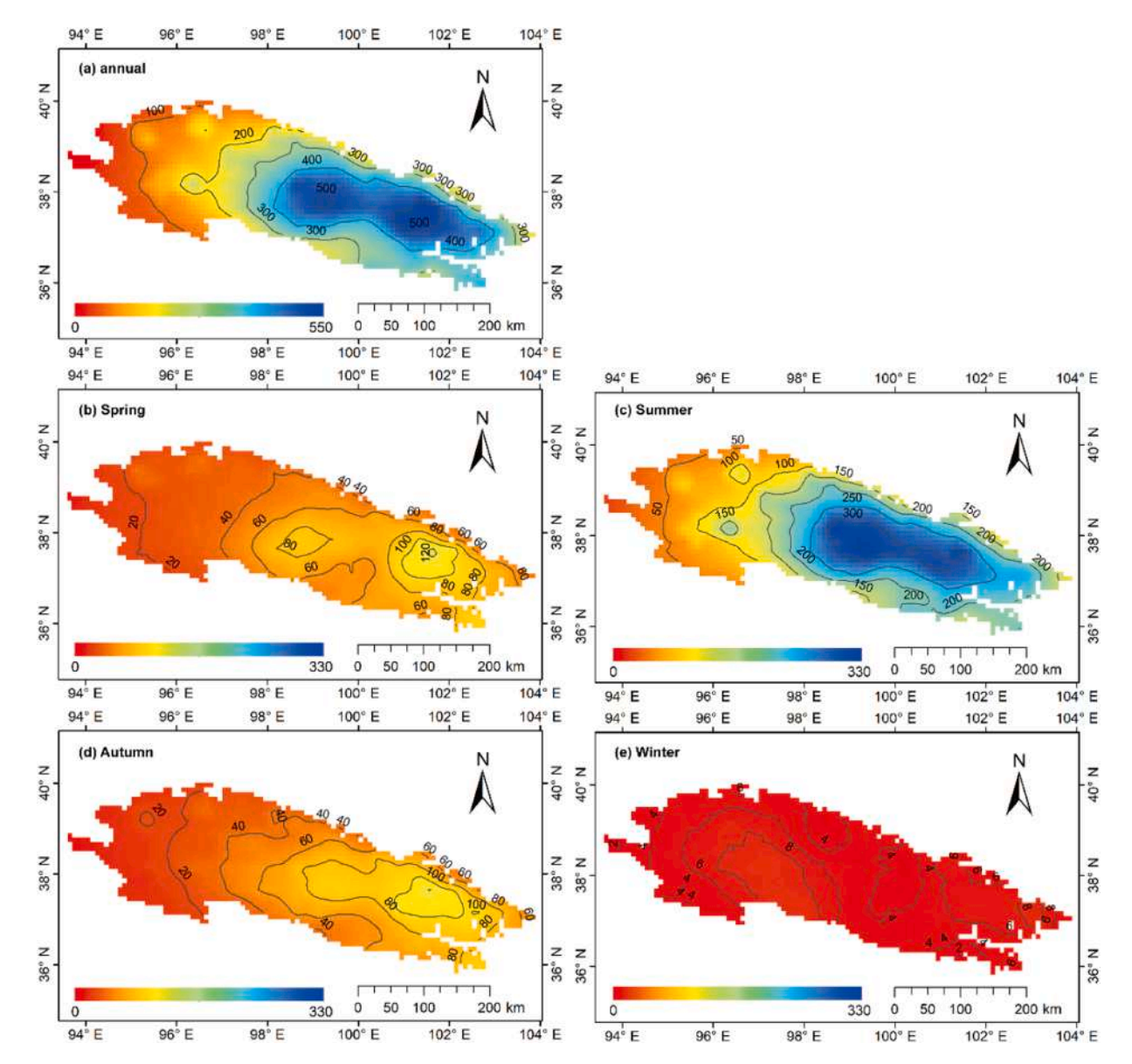


Fig. 5. Spatial distribution of (a) average annual and (b)-(e) seasonal precipitation (mm) in the Qilian Mountains during 1979-2018.

100~m elevation intervals and 0.2° geographical coordinate intervals.

The average annual precipitation in the QM exhibits a generally subtle variation with elevation, following an overall decreasing trend with some fluctuations (Fig. 6a). Within the 2300–2900 m range, precipitation initially decreases before experiencing an increase, with amounts exceeding 300 mm in this altitudinal zone. At higher elevations between 3200–5000 m, average annual precipitation first increases and then decreases, although a slight increase is observed above 4700 m. The latitudinal precipitation gradient appears to remarkably evident (Fig. 6b), showing a clear south-to-north decline. Similarly, the longitudinal profile exhibits distinct spatial patterns (Fig. 6c). Here, precipitation increases from west to east initially, with some fluctuations, before ultimately trending downward.

Compared to the spatial distribution of average annual precipitation, total annual precipitation demonstrates more distinct spatial structuring along geographic gradients. In the QM region, the primary maximum precipitation zone occurs at elevations between 3900–4000 m, with a secondary peak observed between 3100 and 3200 m. These high-precipitation zones are predominately suited within the geographic range of $37.4^{\circ}N$ to $37.6^{\circ}N$ and $99.2^{\circ}E$ to $99.4^{\circ}E$ (Fig. 7). Notably, the majority of precipitation is concentrated within the elevation band of 3100-4200 m (Fig. 7a). Areas above 3000 m account for 80 % of the region's total precipitation, while those above 3600 m contribute 50 %.

In the latitudinal direction (Fig. 7b), total annual precipitation is concentrated between 37°N and 38°N, with values exceeding 3.0×10^9 m³. The latitudinal profile reveals a unimodal distribution pattern, increasing initially and then gradually decreasing with

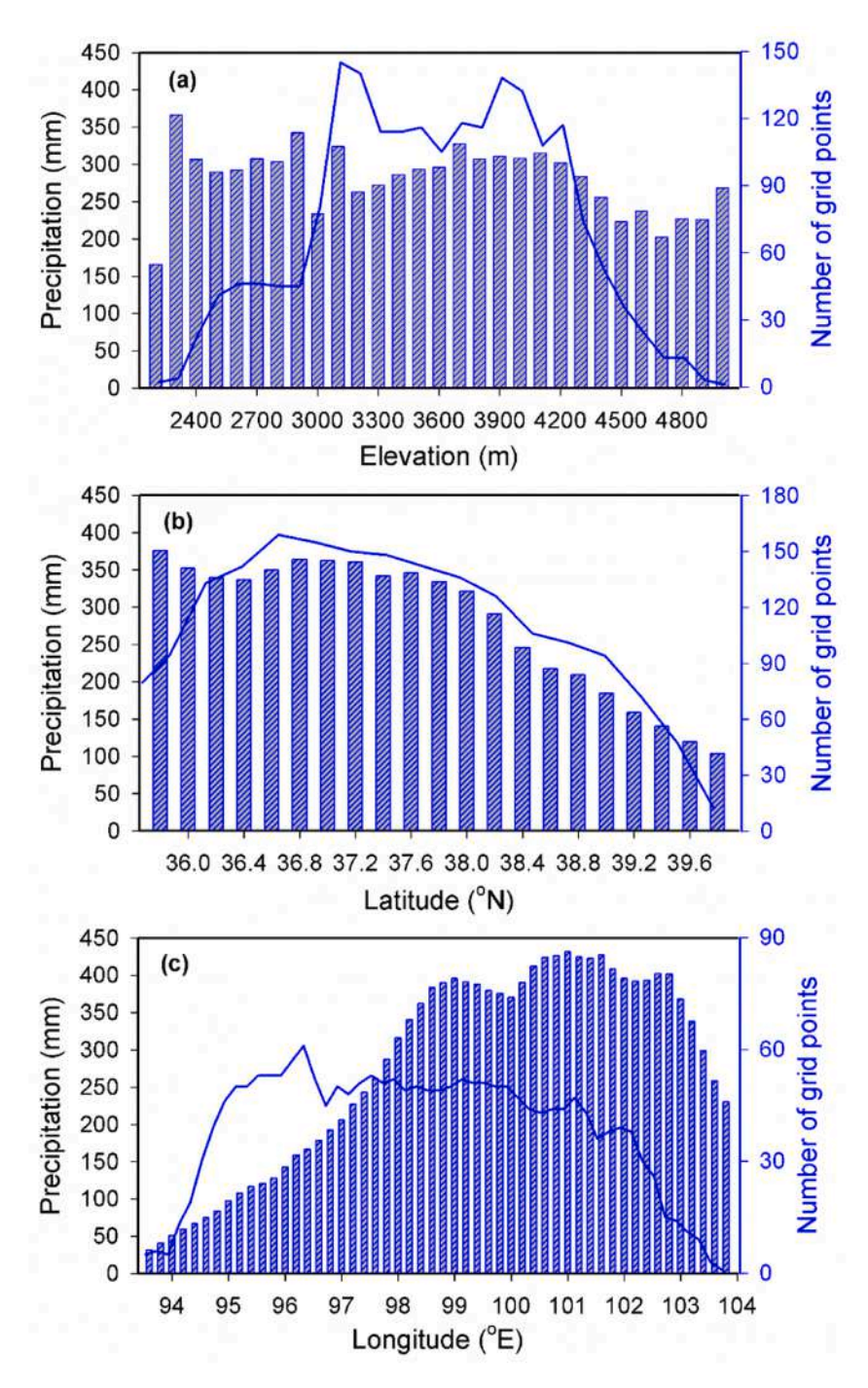


Fig. 6. Average annual precipitation (vertical bar) and the number of grid points (blue curve) in the Qilian Mountains versus (a) elevation, (b) latitude, and (c) longitude.

higher latitudes, peaking between $37.4^{\circ}N$ and $37.6^{\circ}N$. Longitudinally (Fig. 7c), total annual precipitation is primarily distributed between $98.4^{\circ}E$ and $101.2^{\circ}E$. The western sector ($93.6^{\circ}E$ to $99.2^{\circ}E$) exhibits a progressive eastward increase in precipitation. In contrast, the eastern sector ($102.2^{\circ}E$ to $103.8^{\circ}E$) shows an inverse relationship, with total annual precipitation decreasing eastward.

The annual precipitation change rate exhibits a pronounced elevation-dependent amplification across the study area, rising from approximately 2 mm a^{-1} at lower altitudes to around 10 mm a^{-1} at higher elevations (Fig. 8a). In fact, the large increase is located in the western QM, where features high elevations and an arid climate, while the modest increase is observed in the eastern QM, characterized by lower elevations and a semi-humid climate (Fig. 9). This pattern contrasts sharply with the spatial distribution of

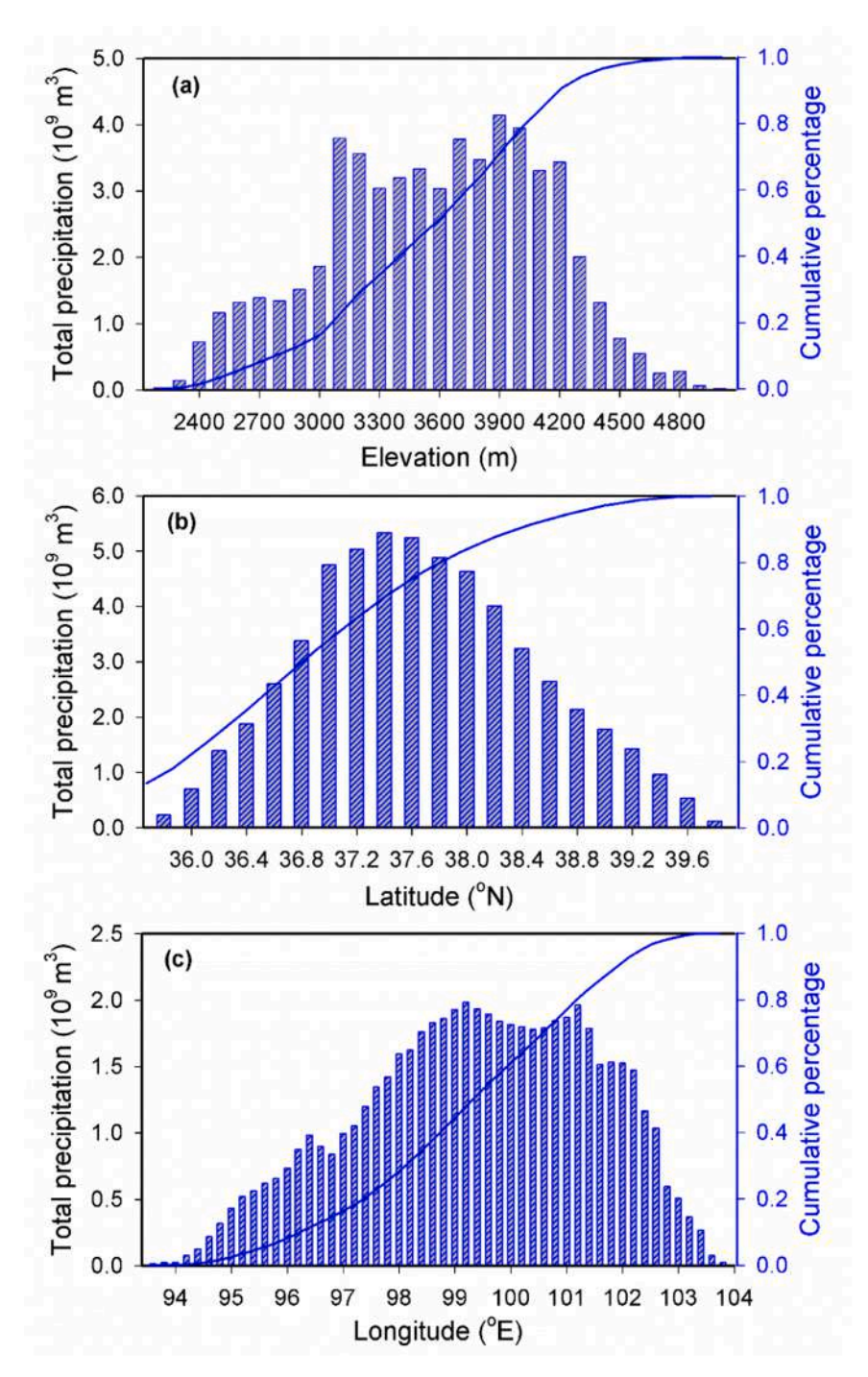


Fig. 7. Total annual precipitation (annual precipitation × area) and cumulative percentage (blue curve) in the Qilian Mountains virus (a) elevation, (b) latitude, and (c) longitude.

mean annual precipitation. These findings align with a previous study on the Tibetan Plateau, which reported that precipitation increased with altitude at a rate of $0.83 \,\%$ decade⁻¹ km ⁻¹ between 1970 and 2014, with a higher rate ($2.23 \,\%$ decade⁻¹ km ⁻¹) from 1991 to 2014 (Li et al., 2017).

The latitudinal gradient exhibits more variable patterns in precipitation variations (Fig. 8b). Between 36.0° N and 36.8° N, the change rate decreases with latitude. This trend reverses northward through 39.2° N, exhibiting a fluctuating behavior. Beyond 39.2° N, a marked decline ensues, reaching a minimum rate of less than 2 mm a⁻¹ at 39.8° N– 40.0° N. The highest interannual variability (3.8 mm a⁻¹) occurs within the narrow band of 39.2° N and 39.4° N, suggesting strengthened climate sensitivity in this transitional

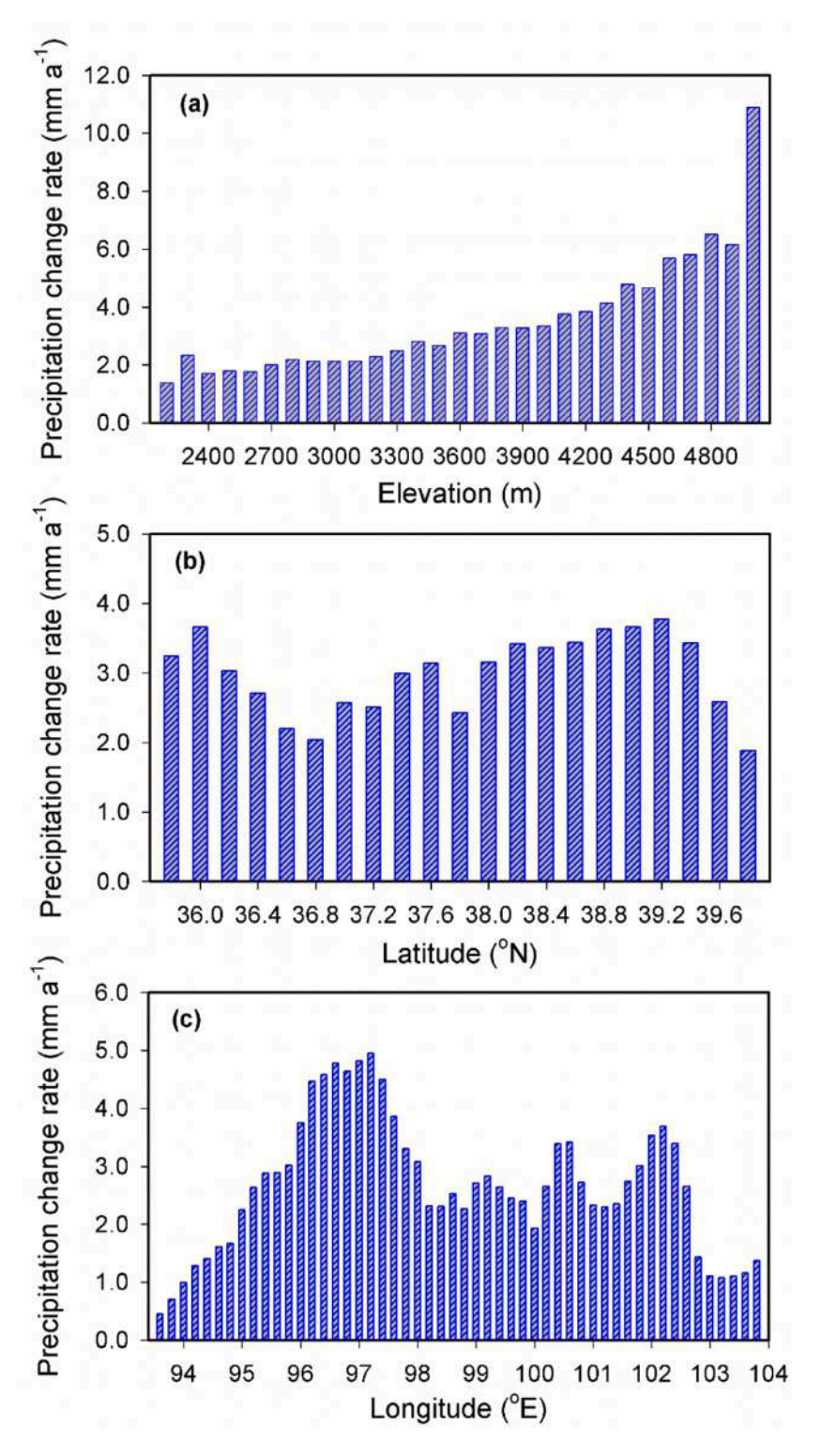


Fig. 8. Annual precipitation change rate versus (a) elevation, (b) latitude, and (c) longitude.

region. Longitudinal profile exhibits more erratic patterns and greater variability than latitudinal counterpart (Fig. 8c). An initial eastward increase peaks at 5 mm a^{-1} between 97.2°E and 97.4°E. Subsequently, it fluctuates downward, ultimately reaching a minimum of 1 mm a^{-1} between 103.2°E and 103.4°E.

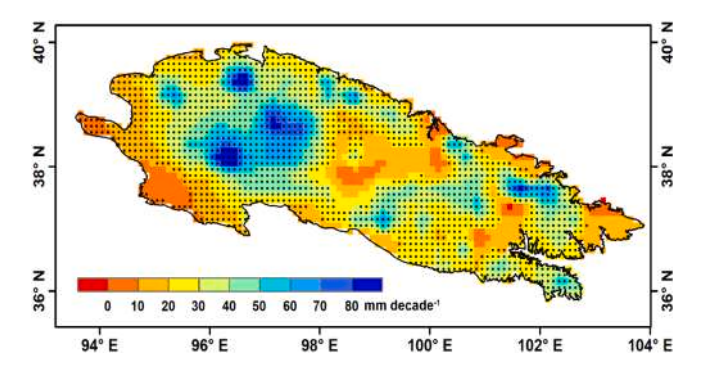


Fig. 9. Spatial distribution of annual precipitation trends in the Qilian Mountains from 1979 to 2018. Dots indicate trends that are statistically significant at the 95 % confidence level.

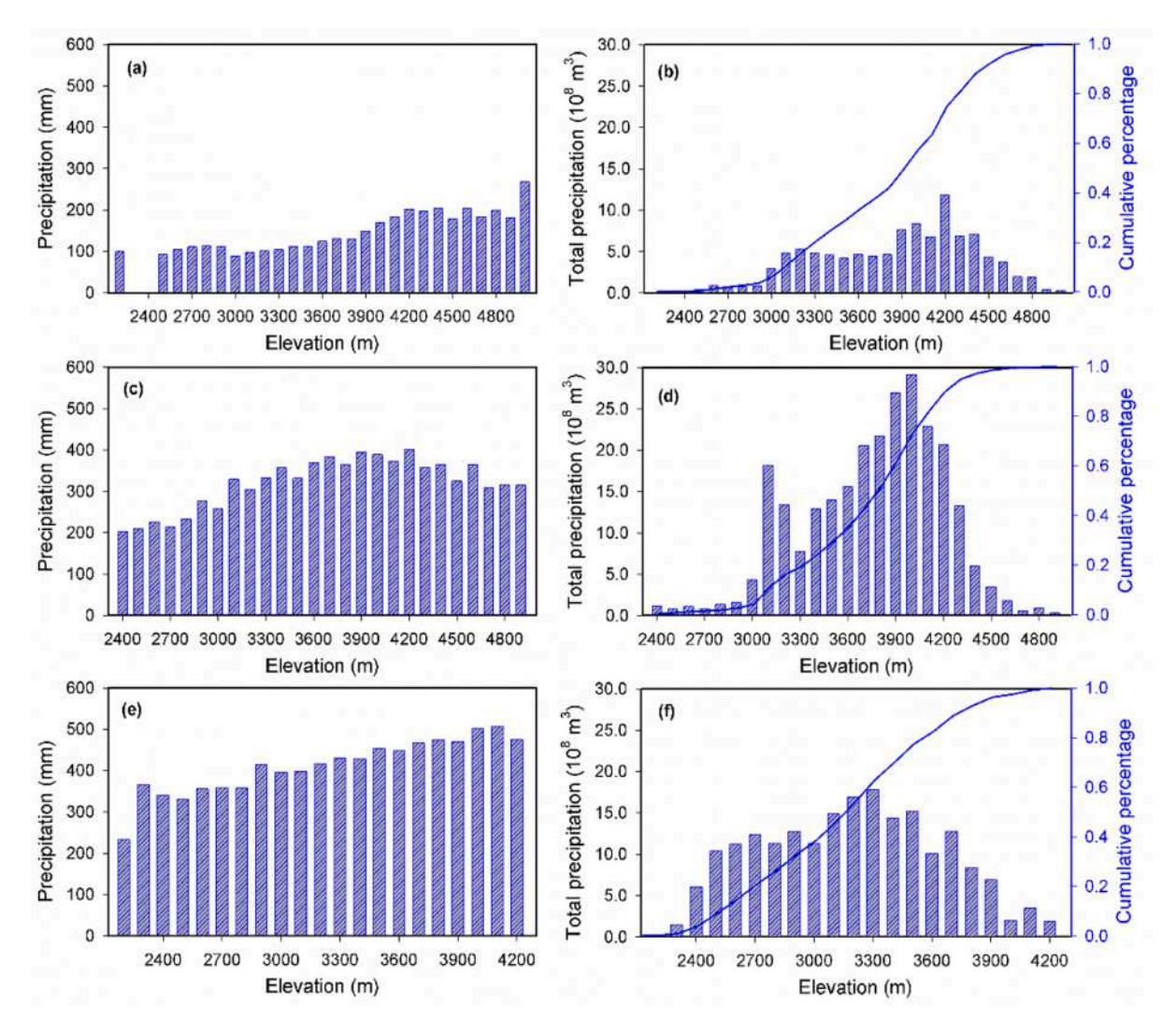


Fig. 10. Variations of annual precipitation and annual total precipitation with elevation in the western (a, b), central (c, d), and eastern (e, f) Qilian Mountains.

3.4. Precipitation variation with elevation across different sub-regions

The spatial distribution of annual precipitation in the QM (Fig. 5) shows a distinct precipitation center in the eastern sector, east of $100^{\circ}30'E$, with a secondary peak centered near $99^{\circ}E$. The 300 mm isohyet lies west of $97^{\circ}30'E$, where mean annual precipitation remains below 300 mm. Therefore, we categorized the QM region into western, central, and eastern sub-regions, using $97^{\circ}30'E$ and $100^{\circ}30'E$ as boundaries, with intervals of approximately 3° longitudinal intervals. Within the classification, the western and central regions have comparable spatial extents in both grid numbers (760 vs 752) and geographical areas ($73488 \text{ km}^2 \text{ vs } 73274 \text{ km}^2$), while the eastern region covers a smaller area (49552 km^2). Topographic analysis reveals an elevational gradient decreasing eastward: the western region has the highest elevation range (2200-5000 m), followed by the central region (2400-5000 m), and while the eastern region exhibits the lowest elevation range (2000-4300 m).

The elevation dependency of annual precipitation in the western region exhibits a generally increasing trend with elevation (Fig. 10a). Between 3000–4200 m, precipitation increases consistently with elevation, while both lower (2500–2900 m) and higher (4300–5000 m) elevation zones exhibit fluctuating precipitation patterns without a clear monotonic trend. Notably, the maximum precipitation zone in the western QM occurs at 4200 m (Fig. 10b), with concentrated annual total precipitation occurring between 3000–4600 m. The cumulative precipitation analysis indicates that elevations above 3300 m account for 80 % of the regional precipitation total, while those above 3900 m contribute 50 %.

For the central region (Fig. 10c), annual precipitation tends to increase with elevation from 2400 to 4200 m, but experiences variable decreases at higher elevations (4200–4800 m). The maximum precipitation zone here is found at 4000 m (Fig. 10d), with precipitation concentrated between 3100–4300 m. Areas above 3550 m collectively account for 80 % of the regional precipitation total, and those above 3750 m contribute 50 %.

In the eastern region (Fig. 10e), annual precipitation shows intermittent increases from 2500 to 4100 m. The maximum precipitation zone shifts downward to 3300 m (Fig. 10f), with concentrated precipitation between 2400–3900 m. Areas above 2700 m dominant precipitation input (80 % of the regional total), while those above 3150 m contribute 50 %.

Overall, across the western, central, and eastern QM, average annual precipitation exhibits a fluctuating yet generally increasing trend with elevation. Three distinct maximum precipitation zones are distributed, each aligned with the topographic features of their respective sub-regions. The central region records the highest total precipitation on average, while the western region hosts the highest elevation for maximum precipitation zone, corresponding to its enhanced topographic lifting effects.

3.5. Spatial distribution of intra-annual precipitation change

To characterize the spatial distribution of intra-annual precipitation variation, we analyzed both average monthly precipitation and monthly total precipitation across different elevation gradients and geographical coordinates (refer to Fig. 11). Average monthly

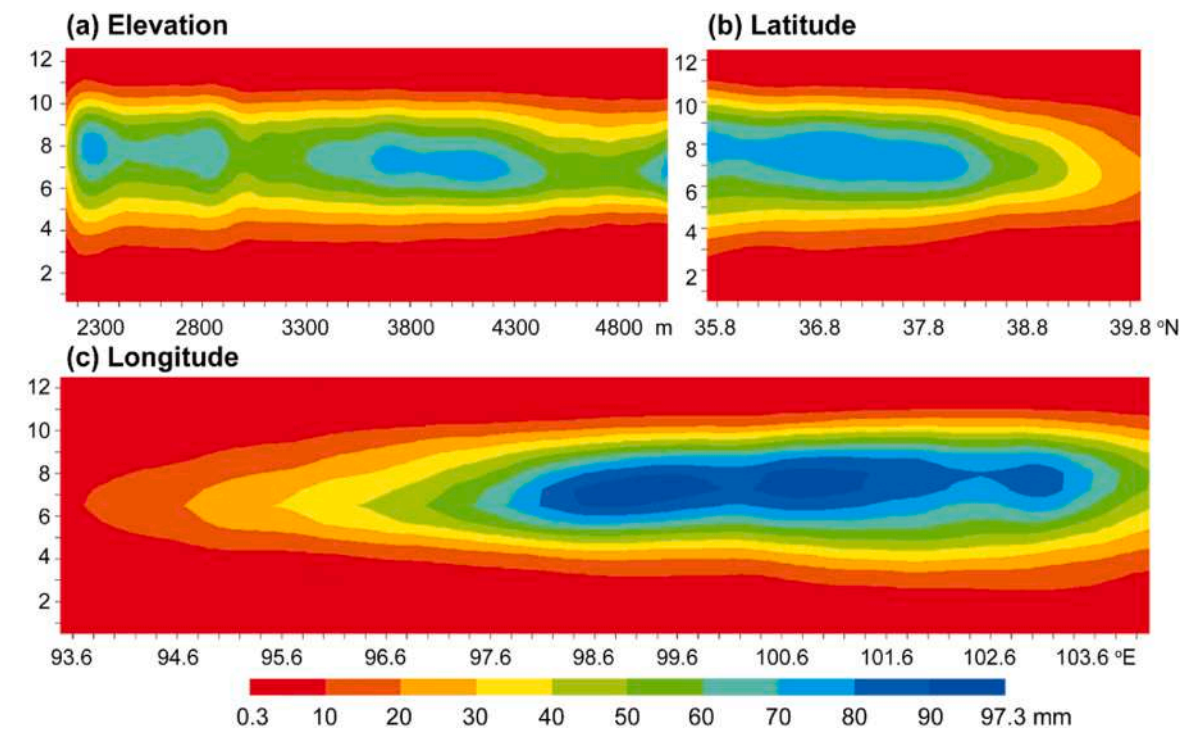


Fig. 11. Spatial distribution of the intra-annual change in average monthly precipitation by (a) elevation, (b) latitude, and (c) longitude.

precipitation is concentrated between May and September across all elevation and geographical gradients, with August being the wettest month. Higher precipitation occurs primarily within two elevation ranges: 2200–2400 m and 3600–4300 m. Geographically, precipitation is concentrated within the ranges of 35.8°N–38.2°N and 98.2°E–103.2°E, respectively. Fig. 11a reveals that in low-altitude areas, the average monthly precipitation remains below 8 mm from October to February of the following year; whereas in high-altitude areas, precipitation is similarly low (below 8 mm) from September to March. Notably, a precipitation center is identified between elevations of 3600–4200 m from May to July. In contrast, the elevation zone of 3000–3100 m receives less monthly precipitation than its surrounding areas, suggesting that this altitude range acts as a transitional buffer between highland and lowland precipitation regimes.

Monthly total precipitation follows a similar spatial and temporal pattern (Fig. 12), also peaking from May to September, with the highest amount in August. The maximum monthly total precipitation is mainly distributed within the elevation range of 3900–4000 m, latitudes between 37.2°N and 37.8°N, and longitudes from 98.2°E to 101.4°E (Fig. 12). A pronounced precipitation center is evident between 3900–4050 m during May to July (Fig. 12a). Overall, both average monthly and total precipitation are predominantly distributed between May and September and are most pronounced at mid-to-high elevations (3700–4200 m).

4. Discussion

4.1. Causes of varying performance of reanalysis datasets

The different performances of the CMFD, CN-1km, LZU0025, and ERA5 can be largely associated with the methodologies involved in their generation and the diversity of data sources incorporated. The CMFD and LZU0025 datasets both adopted the ANU-Spline statistical interpolation method, which introduces linear covariables, such as DEM and slope, into the interpolation process. This approach helps convert disperse stations to high-accuracy, spatially continuous surface, mitigating issues related to limited station density. The CN-1km dataset adopted delta spatial downscaling, a method that capitalizes on statistical relationship inherent in the climate system. It generally uses bias-correlation relationship derived from large-scale climate model outputs (i.e., Global Climate Models) and historical observations, while also incorporating local topographic factors to refine high-resolutions (~1 km) climate scenarios from coarse climate model outputs (50–100 km). EAR5 adopted data assimilation system to integrate extensive observations with atmospheric model outputs to produce its reanalysis estimates. In addition, different data sources used in these datasets further differentiates these datasets. CMFD combined around 1000 weather station data with satellite and reanalysis data, enhancing its robustness through a balance of local and global information. LZU0025, however, relied exclusively on 1202 precipitation stations within China and did not incorporate satellite or reanalysis data. This constrains it ability to correct biases and supply reliable precipitation information in remote regions with sparse station coverage, such as the northeastern Tibetan Plateau. The generation of CN-

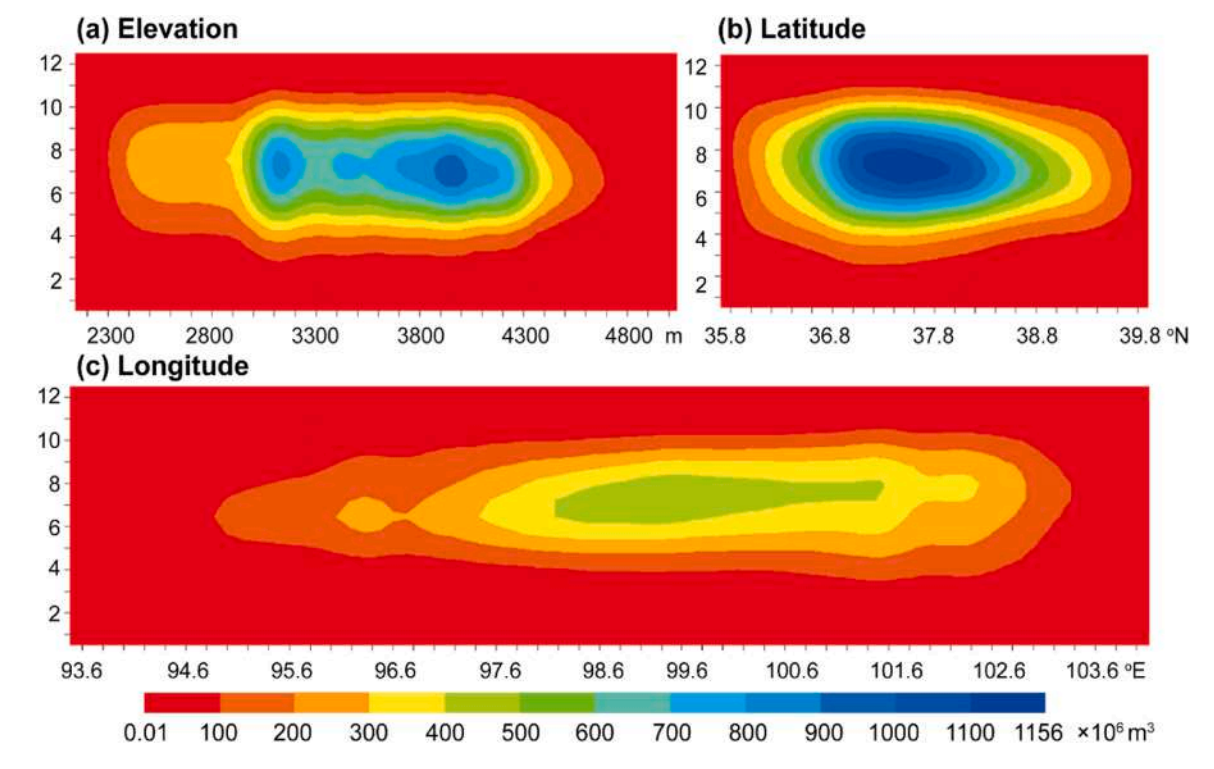


Fig. 12. As in Fig. 11, but for monthly total precipitation calculated as monthly precipitation \times area.

1km is based on the CRU dataset—which adopted the national meteorological stations in China—and the WorldClim global climate dataset. Although it was validated using 496 independent Chinese meteorological stations, its generation in globally downscaled data may smooth local details, especially in high-elevation areas. ERA5 also integrated model outputs and multiple sources of observations; however, its representation above 1.5 km elevation remains limited (Orsolini et al., 2019), leading to higher uncertainty in high-altitude regions such as the QM on the northeastern Tibetan Plateau. Given that the accuracy of precipitation products considerably affects the performance of hydrological models in streamflow simulations (Li et al., 2025b), developing high-accuracy, topographically sensitive precipitation datasets is essential for reliable applications in mountainous regions.

4.2. Spatiotemporal variability of precipitation: Comparison with previous studies, causes, and hydrological implications

The QM exhibits a distinct east-west precipitation gradient, characterized by higher moisture availability in the eastern regions and increasing aridity towards the west, along with uneven seasonal distribution. This pattern aligns with previously documented climatic patterns (Jia et al., 2008; Wang et al., 2018b; Sun et al., 2019; Li et al., 2025b). Notably, temporal precipitation trends reveal a contrasting spatial pattern: eastern parts of the QM demonstrate a modest increase, while the western areas show more significant increases during the study period. A similar pattern is observed in the upper Yellow River Basin (Zhang et al., 2023), where arid northwestern areas show an apparent precipitation increase, and semi-humid eastern regions experienced significant decreases.

The spatial variability of precipitation in the QM is complex, governed by interactions among the mid-latitude westerlies, the Asian monsoon, and local topography. As a crucial topographic barrier in western China, the QM intercepts mid-latitude westerlies laden with moisture from the Atlantic Ocean and Eurasia (Li et al., 2015; Wang et al., 2018b). Topographic lifting creates pronounced precipitation disparities, with western slopes receiving less rainfall than eastern ones due to rain-shadow effects, amplifying the east-west precipitation contrast. In contrast, the eastern QM benefits from greater moisture influx through summer monsoon precipitation and recycled precipitation from local and surroundings. Recent studies indicate that over the past few decades, intensified westerly circulation coupled with a weakening monsoon system has led to increased precipitation in the westerly-dominated areas of the Tibetan Plateau, while monsoon-dominated regions have witnessed a decrease in precipitation (Wang et al., 2018a; Yao et al., 2022; Jiang et al., 2023).

In our previous study (Wang et al., 2018b), dynamic diagnostics based on multi-source reanalysis datasets and water vapor transport budgets revealed two key patterns. Climatologically, the meridional water vapor budget contributes positively to regional water vapor budget and precipitation, while the zonal budget exhibits a negative contribution. Temporally, the zonal water vapor budget has strengthened, whereas meridional component has weakened. This shift has resulted in an overall increase in net regional water vapor budget and precipitation. Fig. 13 shows the correlations between annual precipitation in the QM and several large-scale climate oscillation indices. A significant positive correlation is identified with the AMO (at the 95 % confidence level), while negative—though statistically insignificant—correlations appear with the MEI and SASMI. These correlations suggest that the AMO acts as an important remote driver of interannual precipitation variability in the QM. Specifically, the transition toward a positive AMO phase since the 1990s has triggered an atmospheric wave train, leading to an upper-level anticyclonic circulation anomaly over the Mongolia Plateau (Wu et al., 2022; Liu et al., 2024). This circulation pattern critically modulates large-scale atmospheric dynamics, notably contributing to a weakened Asian summer monsoon (Wu et al., 2022). Consequently, the QM has experienced enhanced influence from

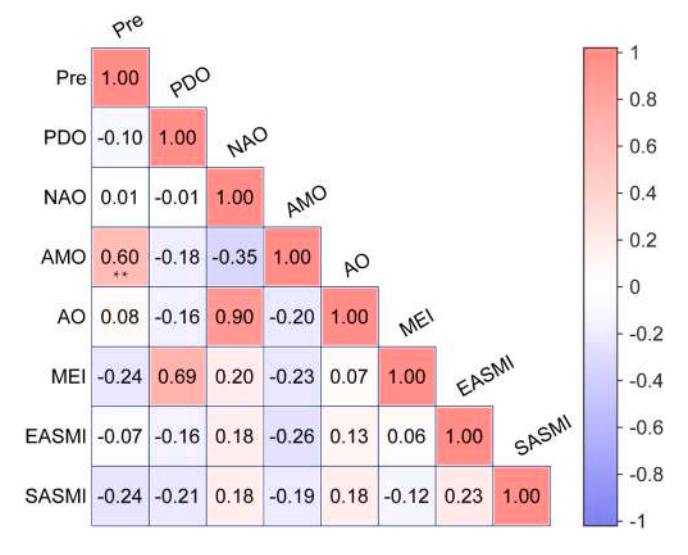


Fig. 13. Heatmap of correlation coefficients between annual precipitation (Pre) in the QM and large-scale climate oscillation indices from 1979 to 2018. PDO: Pacific Decadal Oscillation; NAO: North Atlantic Oscillation; AMO: Atlantic Multi-decadal Oscillation; AO: Arctic Oscillation; MEI: Multivariate ENSO Index; EASMI: East Asian Summer Monsoon Index; SASMI: South Asian Summer Monsoon Index. ** indicates the correlation coefficient passed the 95 % confidence level.

anomalous easterly water vapor transport (Liu et al., 2024), originating from the Arctic and North Pacific Oceans (Wu et al., 2022). This teleconnection mechanism reinforces zonal moisture convergence and increase overall moisture supply, thereby supporting the observed decadal-scale increase in precipitation in the QM. In contrast, the weakening of the South Asian Monsoon appears unfavorable for precipitation increase in this region.

During the positive phase of MEI, denoting the warm phase of ENSO, the sea surface temperature gradient between the eastern and western Pacific Ocean reduces. This leads to a weakened Walker Circulation and a decrease in the intensity of the western Pacific subtropical high, typically accompanied by a southward displacement of the high-pressure system (Lu et al., 2019). As a result, the westerlies exert stronger influence over the western QM, prompting enhanced precipitation in that area.

As a crucial component of the hydrological cycle, changes in precipitation patterns considerably affect the QM's runoff. In response to a modest increase in precipitation over the eastern QM, the annual runoff of the Shiyang, Huangshui, Datong, and Zhuanglang Rivers showed downward trends. Conversely, annual runoff in the western QM (e.g., Shule and Danghe Rivers) exhibited upward trends, concurrent with rising precipitation in that region. Central QM's annual runoff exhibited mixed trends, the Heihe River increased while Beida River decreased, although experiencing a slight increasing precipitation (Liu et al., 2023), suggesting the factors (i.e., evapotranspiration and human activities) other than precipitation have been significantly influencing runoff trends here. These results further support the reliability of the spatial distribution pattern of interannual precipitation changes in the QM.

The primary maximum precipitation zone in the QM occurs between 3900 and 4000 m, with distinct spatial heterogeneity along the mountain range. Our analysis reveals a westward ascending pattern of maximum precipitation zone across the QM: 3300 m in the east, 4000 m in the center, and 4200 m in the west. The spatial gradient aligns with previous results from Sun et al. (2019), who used TRMM satellite precipitation data (eastern: 4100 m; central: 4500 m; western: 4700 m), although our estimates suggest relative lower elevations. The discrepancy may be due to methodological differences in elevation binning and spatial averaging approaches. Huang et al. (2020) obtained a maximum precipitation zone around 3000 m in the eastern QM through GSOD (Global Surface Summary of the Day) ground precipitation data corrected MSWEP (Multi-Source Weighted-Ensemble Precipitation) data, which is slightly lower than our estimate of 3300 m. This divergence may stem from topographic differences across the eastern regions and the use of different precipitation datasets. Intriguingly, a study report absence of distinct maximum precipitation zone in high-elevation QM areas despite increasing precipitation with altitude (Geng et al., 2017), potentially because of insufficient moisture availability at high altitudes and high local lifting condensation levels, limiting topographic precipitation effects. Besides, the formation of maximum precipitation zone appears to be governed by vertical atmospheric coupling. Diagnostic analyses indicate that the emergence of maximum precipitation zone in the QM is closely associated with the heights of two relative humidity centers in upper and lower atmospheric layers and corresponding strong cold air convection centers (Li et al., 2010).

Mountains significantly enhance precipitation via orographic lifting, but their contribution is misrepresented without area integration. Methodologically, our estimation of the maximum precipitation zone differs from previous studies by implementing elevation-dependent area weighting (Fig. 7), which account for non-uniform distribution of topographic grids. This approach provides a better representation of regional water availability (Qiang et al., 2016), as it integrates both precipitation amount and the contributing area within specific elevation zones. In mountainous terrain, higher elevations typically exhibit greater water availability because of orographic enhancement of precipitation. These zones often generate net positive water volumes, serving as primary recharge zones for groundwater, while low-lying areas act as discharge zones. Besides, the contributing area varies with elevation zone. By dividing the QM into elevation zones, we can account for the orographic precipitation effect and the variation in contributing area. This zonal approach is crucial for a detailed and accurate representation of regional water availability and for evaluating water supply to dependent ecosystems.

4.3. Limitations of this study and future research directions

This study conducted a systematic evaluation of precipitation characteristics in the QM using the CMFD data, with a focus on spatiotemporal variability and elevation dependency. The analysis is based on CMFD data covering the period from 1979 to 2018. Although a more recent version (CMFD v2.0) has been released, extending the temporal span from 1951 to 2024 and integrating the ERA5 reanalysis data with meteorological station observations, as well as artificial intelligence techniques to merge radiation data from ISCCP-ITP-CNN and precipitation data from TPHiPr (Yang et al., 2019). The data generation methods and data sources in CMFD v2.0 differ significantly from those of the version used in this study. In a related study, we used this updated CMFD v2.0 to investigate changes in precipitation days and amounts in the QM from 1979 to 2024 (Wang et al., 2025). While the overall precipitation trends are broadly consistent between the both versions—exhibiting a more pronounced increase in the western QM and a moderate increase in eastern areas—certain discrepancies remain. These include a drying trend in the eastern QM region and differences in the magnitude of trends. These differences likely stem from differences in assimilated data sources and data generation methods (He et al., 2020; Yang et al., 2019), as well as recent changes in precipitation patterns.

The region's complex geographical conditions lead to highly uneven distribution of meteorological stations, potentially compromising the accuracy of precipitation dataset evaluations. To advance understanding of orographic precipitation mechanisms in the QM, future studies should integrate multi-dimensional analyses including the following key aspects: (1) quantitative assessment of land surface-atmosphere interactions through high-resolution climate modeling, with specific focus on the influence of the slope aspect; (2) analysis of vegetation-climate feedbacks using remote sensing indices and dynamic vegetation models; and (3) dynamic tracking of moisture transport pathways by means of atmospheric reanalysis dataset and moisture trajectory models. Current research remains limited in explaining mechanistic drivers of spatial precipitation variability. We propose establishing a weighted contribution index to disentangle the synergistic effect of terrain forcing and atmospheric circulations on precipitation patterns. This could

significantly improve the simulation ability of regional climate models and hydrological models in mountainous environments. Another limitation lies in the current focus on annual-scale precipitation-elevation relationships. Future studies should investigate these relationships at seasonal or monthly scales to better elucidate the complex mechanisms of orographic precipitation and its impact on hydrological processes and water resources, given that the precipitation and hydrological supply in the region are concentrated during the wet season (May to September) and there may exit seasonal variations of the maximum precipitation zone (Wang et al., 2009).

5. Conclusions

This study evaluated precipitation data from four gridded products, i.e., China Meteorological Forcing Dataset (CMFD), long-term high-resolution monthly climate dataset (LZU0025), China 1 km resolution monthly precipitation dataset, and ERA5 reanalysis data with observations from 30 meteorological stations. We found that the CMFD data best represents precipitation variations in the QM. Validation using data from five independent *in-situ* stations further confirmed the CMFD's high reliability, although with a minor overestimation.

According to the CMFD data, the change rate of annual precipitation in the QM shows considerable spatial heterogeneity. Generally, regions in the west, characterized by an arid climate and higher elevations, exhibit higher change rates, while in the eastern areas, with a semi-humid climate and lower elevation, show relatively lower rates, which contrast with the spatial distribution of average annual precipitation. Furthermore, the annual precipitation change rate in the QM exhibits a clear elevational dependence—the increase in precipitation increases with elevation, while average annual precipitation tends to decline with increasing elevation. The zone of maximum precipitation in the QM is located between 3900–4000 m, followed by 3100–3200 m, within the geographical coordinates of 37.4°N–37.5°N and 99.2°E–99.4°E.

Across the three sub-regions of the QM—western, central, and eastern—the average annual precipitation increases with elevation in the range of 3000–4200 m. Each sub-region features distinct maximum precipitation zones, occurring at elevation of 3300 m in the east, 4000 m in the center, and 4200 m in the west, demonstrating a westward ascending pattern of maximum precipitation zone.

Both average monthly precipitation and total precipitation are highly concentrated during May to September, particularly in midto-high altitude regions (3700–4200 m). The interannual precipitation variability and average annual precipitation show minimal longitudinal and latitudinal gradients, suggesting dominant topographic modulation over geographic coordinates.

CRediT authorship contribution statement

Xuejia Wang: Conceptualization, Writing – original draft, Visualization, Validation, Software, Methodology, Investigation, Formal analysis, Data curation, Project administration. Kun Wang: Writing – review & editing, Formal analysis, Visualization. Jiayu Wang: Writing – review & editing. Yue Yuan: Writing – review & editing. Guojin Pang: Writing – review & editing, Investigation, Visualization, Funding acquisition. Xiaohua Gou: Writing – review & editing, Methodology, Funding acquisition. Yijia Li: Writing – review & editing. Qi Wang: Writing – review & editing. Lanya Liu: Writing – review & editing, Investigation, Resources. Baktybek Duisebek: Writing – review & editing. Yermekov Farabi Kerimbayevich: Writing – review & editing, Funding acquisition. Meixue Yang: Writing – review & editing, Resources.

Declaration of Competing Interest

The authors declare that they have no known competing financial interests or personal relationships that could have appeared to influence the work reported in this paper.

Acknowledgements

This study was jointly funded by the National Natural Science Foundation of China (42477483, U21A2006, 42161025), the Science Committee of the Ministry of Science and Higher Education of the Republic of Kazakhstan (BR2499322), the Central Government Guiding Local Science and Technology Development Funds (25ZYJA019), and the Start-up Funds for Introduced Talent at Lanzhou University (561120217). This work was supported by the Supercomputing Center of Lanzhou University.

Appendix A. Supporting information

Supplementary data associated with this article can be found in the online version at doi:10.1016/j.ejrh.2025.102821.

Data availability

Data will be made available on request.

References

- Chen, L., Brun, P., Buri, P., Fatichi, S., Gessler, A., McCarthy, M.J., Pellicciotti, F., Stocker, B., Karger, D.N., 2025. Global increase in the occurrence and impact of multiyear droughts. Science 387 (6731), 278–284 https://doi.org/abs/10.1126/science.ado4245.
- Chen, R., Li, H., Wang, X., Gou, X., Yang, M., Wan, G., 2022. Surface air temperature changes over the Tibetan plateau: historical evaluation and future projection based on CMIP6 models. Geosci. Front. 13 (6), 101452. https://doi.org/10.1016/j.gsf.2022.101452.
- Cheng, P., Kong, X., Luo, H., Li, B., Wang, Y., 2020. Climate change and its runoff response in the middle section of the Qilian Mountains in the past 60 years. Arid Land Geogr. 43 (05), 1192–1201. https://doi.org/10.12118/j.issn.1000 6060.2020.05.04.
- Deng, H.X., Tang, Q.H., Yun, X.B., Tang, Y., Liu, X.C., Xu, X.M., Sun, S.A., Zhao, G., Zhang, Y.Y., Zhang, Y.Q., 2022. Wetting trend in northwest China reversed by warmer temperature and drier air. J. Hydrol. 613. https://doi.org/10.1016/j.jhydrol.2022.128435.
- Geng, H., Pan, B., Huang, B., Cao, B., Gao, H., 2017. The spatial distribution of precipitation and topography in the qilian shan mountains, northeastern Tibetan plateau. Geomorphology 297, 43–54. https://doi.org/10.1016/j.geomorph.2017.08.050.
- Gou, X., Deng, Y., Gao, L., Chen, F., Cook, E., Yang, M., Zhang, F., 2015. Millennium tree-ring reconstruction of drought variability in the eastern Qilian Mountains, northwest China. Clim. Dyn. 45 (7), 1761–1770. https://doi.org/10.1007/s00382-014-2431-y.
- Han, X., Xue, H., Zhao, C., Lu, D., 2016. The roles of convective and stratiform precipitation in the observed precipitation trends in northwest China during 1961–2000. Atmos. Res. 169, 139–146. https://doi.org/10.1016/j.atmosres.2015.10.001.
- He, J., Yang, K., Tang, W., Lu, H., Qin, J., Chen, Y., Li, X., 2020. The first high-resolution meteorological forcing dataset for land process studies over China. Sci. data 7 (1), 25. https://doi.org/10.1038/s41597-020-0369-y.
- Hersbach, H., Bell, B., Berrisford, P., Hirahara, S., Horányi, A., Muñoz-Sabater, J., Nicolas, J., Peubey, C., Radu, R., Schepers, D., Simmons, A., Soci, C., Abdalla, S., Abellan, X., Balsamo, G., Bechtold, P., Biavati, G., Bidlot, J., Bonavita, M., De Chiara, G., Dahlgren, P., Dee, D., Diamantakis, M., Dragani, R., Flemming, J., Forbes, R., Fuentes, M., Geer, A., Haimberger, L., Healy, S., Hogan, R.J., Hólm, E., Janisková, M., Keeley, S., Laloyaux, P., Lopez, P., Lupu, C., Radnoti, G., de Rosnay, P., Rozum, I., Vamborg, F., Villaume, S., Thépaut, J.-N., 2020. The ERA5 global reanalysis. Q. J. R. Meteorol. Soc. 146 (730), 1999–2049. https://doi.org/10.1002/gi.3803.
- Huang, Q., Tan, G., Wang, R., Xiang, J., Hu, Q., Li, L., 2020. Analysis of spatial distribution characteristics of precipitation in Qilian Mountains based on MSWEP. J. Hydraul. Eng. 51 (2), 232–244. https://doi.org/10.13243/j.cnki.slxb.20190876.
- Huang, X., Zhang, M., Jia, W., Wang, S., Zhang, N., 2011. Variations of surface humidity and its influential factors in northwest China. Adv. Water Sci. 22 (02), 151–159. https://doi.org/10.14042/j.cnki.32.1309.2011.02.014.
- IPCC, 2021. In: Masson-Delmotte, V., Zhai, P., Pirani, A., et al. (Eds.), Climate Change 2021: The Physical Science Basis. Cambridge University Press. https://doi.org/10.1017/9781009157896.
- Ji, F., Wu, Z., Huang, J., Chassignet, E.P., 2014. Evolution of land surface air temperature trend. Nat. Clim. Change 4 (6), 462–466. https://doi.org/10.1038/nclimate2223
- Jia, W., He, Y., Li, Z., Pang, H., Yuan, L., Ning, B., Song, B., Zhang, N., 2008. The regional difference and catastrophe of climatic change in Qilian Mt. Region. Acta Geogr. Sin. 63 (3), 257–269.
- Jiang, J., Zhou, T., Qian, Y., Li, C., Song, F., Li, H., Chen, X., Zhang, W., Chen, Z., 2023. Precipitation regime changes in high mountain Asia driven by cleaner air. Nature 623 (7987), 544–549. https://doi.org/10.1038/s41586-023-06619-y.
- Lalande, M., Ménégoz, M., Krinner, G., et al., 2021. Climate change in the high mountain Asia in CMIP6. Earth Syst. Dynam 12, 1061–1098. https://doi.org/10.5194/esd-12-1061-2021
- Li, X., Gou, X., Wang, N., Sheng, Y., Jin, H., Qi, Y., Song, X., Hou, F., Li, Y., Zhao, C., 2019. Tightening ecological management facilitates Green development in the Qilian Mountains. Chin. Sci. Bull. 64 (27), 2928–2937. https://doi.org/10.1360/TB-2019-0209.
- Li, X., Wang, L., Guo, X., Chen, D., 2017. Does summer precipitation trend over and around the Tibetan Plateau depend on elevation? Int. J. Climatol. 37 (S1), 1278–1284. https://doi.org/10.1002/joc.4978.
- Li, Y., Wang, X., Gou, X., Wang, Q., Ou, T., Pang, G., Yang, M., Liu, L., Qie, L., Wang, T., Wang, J., Wei, S., Cheng, X., 2025a. Evaluation of the performance of WRF9km in simulating climate over the upper Yellow River basin. Adv. Clim. Change Res. 16 (1), 58–72. https://doi.org/10.1016/j.accre.2024.12.003.
- Li, Y., Yang, M., Wan, G., Man, Y., Wang, X., 2025b. Coupled statistical analysis and hydrological simulation to evaluate the performance of satellite and reanalysis precipitation products in the Qilian Mountains, northwest China. Clim. Dyn. 63 (2), 134. https://doi.org/10.1007/s00382-025-07607-w.
- Li, Y., Zhang, Q., Xu, X., Ma, Y., 2010. Relationship between precipitation and terrain over the Qilian Mountains and their ambient areas. J. Glaciol. Geocryol. 32 (21), 56–61.
- Li, Z., Gao, Y., Wang, Y., Pan, Y., Li, J., Chen, A., Wang, T., Han, C., Song, Y., T.W, H., 2015. Can monsoon moisture arrive in the Qilian Mountains in summer. Quat. Int. 358, 113–125. https://doi.org/10.1016/j.quaint.2014.08.046.
- Lin, Z., 1995. Orographic precipitation climatology. Science Press, Beijing.
- Liu, L., Gou, X., Wang, X., Yang, M., Wei, S., Pang, G., Qie, L., Li, Y., Wang, Q., Wang, T., Jin, X., 2024. The increases in extreme climatic events over the northeastern Tibetan plateau and their association with atmospheric circulation changes. Atmos. Res. 304, 107410. https://doi.org/10.1016/j.atmosres.2024.107410.
- Liu, L., Wang, X., Gou, X., Yang, M., Zhang, Z., 2022. Projections of surface air temperature and precipitation in the 21st century in the Qilian Mountains, northwest China, using REMO in the CORDEX. Adv. Clim. Change Res. 13 (3), 344–358. https://doi.org/10.1016/j.accre.2022.03.003.
- Liu, Z., Wang, N., Cuo, L., Liang, L., 2023. Characteristics and attribution of spatiotemporal changes in Qilian Mountains' runoff over the past six decades. J. Geophys. Res. Atmospheres 128 (22), e2023JD039176. https://doi.org/10.1029/2023JD039176.
- Long, B., Zhang, B., He, C., Shao, R., Tian, W., 2018. Is there a change from a warm-dry to a warm-wet climate in the inland river area of China? Interpretation and analysis through surface water balance. J. Geophys. Res. Atmospheres 123 (14), 7114–7131. https://doi.org/10.1029/2018JD028436.
- Lu, B., Li, H., Wu, J., Zhang, T., Liu, J., Liu, B., Chen, Y., Baishan, J., 2019. Impact of el Niño and Southern oscillation on the summer precipitation over northwest China. Atmos. Sci. Lett. 20 (8), e928. https://doi.org/10.1002/asl.928.
- Orsolini, Y., Wegmann, M., Dutra, E., Liu, B., Balsamo, G., Yang, K., de Rosnay, P., Zhu, C., Wang, W., Senan, R., Arduini, G., 2019. Evaluation of snow depth and snow cover over the Tibetan plateau in global reanalyses using in situ and satellite remote sensing observations. Cryosphere 13 (8), 2221–2239. https://doi.org/10.5194/tc-13-2221-2019.
- Peng, S., Ding, Y., Liu, W., Li, Z., 2019. 1 km monthly temperature and precipitation dataset for China from 1901 to 2017. Earth Syst. Sci. Data 11 (4), 1931–1946. https://doi.org/10.5194/essd-11-1931-2019.
- Qiang, F., Zhang, M., Wang, S., Liu, Y., Ren, Z., Zhu, X., 2016. Estimation of areal precipitation in the Qilian Mountains based on a gridded dataset since 1961. J. Geogr. Sci. 26 (1), 59–69. https://doi.org/10.1007/s11442-016-1254-7.
- Shi, Y., 2002. A preliminary study of signal, impact and foreground of climatic shift from warm-dry to warm-humid in northwest China. J. Glaciol. Geocryol. 24 (3), 219–226.
- Shi, Y., Shen, Y., Li, D., Zhang, G., Ding, Y., Hu, R., Kang, E., 2003. Discussion on the present climate change from warm-dry to warm-wet in northwest China. Quat. Sci. 23 (2), 152–164.
- Sun, M., Liu, S., Yao, X., Guo, W., Xu, J., 2015. Glacier changes in the Qilian Mountains in the past half century: based on the revised first and second Chinese glacier inventory. Acta Geogr. Sin. 70 (9), 1402–1414. https://doi.org/10.11821/dlxb201509004.
- Sun, M., Zhang, H., Gong, N., et al., 2019. Study on maximum precipitation height zone in Qilian Mountains area based on TRRM precipitation data. J. Nat. Res. 34, 646–657. https://doi.org/10.31497/zrzyxb.20190317.
- Tang, M., 1985. Geographical distribution of precipitation in Qilian Mountains. Acta Geogr. Sin. 40 (04), 323-332.
- Wang, L., Chen, R., Han, C., Wang, X., Liu, G., Song, Y., Yang, Y., Liu, J., Liu, Z., Liu, X., Guo, S., Zheng, Q., 2019. Change characteristics of precipitation and temperature in the Qilian Mountains and hexi oasis, northwestern China. Environ. Earth Sci. 78 (9), 284. https://doi.org/10.1007/s12665-019-8289-x.

- Wang, N., He, J., Jiang, X., Song, G., Pu, J., Wu, X., Chen, L., 2009. Study on the zone of maximum precipitation in the north slopes of the central Qilian Moutains. J. Glaciol. Geocryol. 31 (3), 395–403. https://doi.org/10.7522/j.issn.1000-0240.2009.0055.
- Wang, X., Chen, D., Pang, G., Gou, X., Yang, M., 2021. Historical and future climates over the upper and middle reaches of the Yellow River basin simulated by a regional climate model in CORDEX. Clim. Dyn. 56 (9), 2749–2771. https://doi.org/10.1007/s00382-020-05617-4.
- Wang, X., Pang, G., Yang, M., 2018a. Precipitation over the Tibetan plateau during recent decades: a review based on observations and simulations. Int. J. Climatol. 38 (3), 1116–1131. https://doi.org/10.1002/joc.5246.
- Wang, X., Pang, G., Yang, M., Wan, G., Liu, Z., 2018b. Precipitation changes in the Qilian Mountains associated with the shifts of regional atmospheric water vapour during 1960–2014. Int. J. Climatol. 38 (12), 4355–4368. https://doi.org/10.1002/joc.5673.
- Wang, X., Wang, J., Wang, K., Gou, X., Yuan, Y., Pang, G., Liu, L., Li, Y., Wang, Q., Wang, T., Munaitpassova, A., Yang, M., Duisebek, B., 2025. Changing characteristics of precipitation days and amounts in the Oilian Mountains during the past four decades and possible causes. J. Geogr. Sci. Under Review.
- Wu, P., Liu, Y., Ding, Y., Li, X., Wang, J., 2022. Modulation of sea surface temperature over the north atlantic and Indian-Pacific warm pool on interdecadal change of summer precipitation over northwest China. Int. J. Climatol. 42 (16), 8526–8538. https://doi.org/10.1002/joc.7743.
- Yang, K., He, J., Tang, W., Qin, J., Cheng, C.C.K., 2010. On downward shortwave and longwave radiations over high altitude regions: observation and modeling in the Tibetan plateau. Agric. For. Meteorol. 150 (1), 38–46. https://doi.org/10.1016/j.agrformet.2009.08.004.
- Yang, K., He, J., Tang, W., Lu, H., Qin, J., Chen, Y., Li, X., 2019. China meteorological forcing dataset v1.6 (1979-2018). Natl. Tibet. Plateau/Third Pole Environ. Data Cent. https://doi.org/10.11888/AtmosphericPhysics.tpe.249369.file.
- Yao, J., Chen, Y., Zhao, Y., Guan, X., Mao, W., Yang, L., 2020. Climatic and associated atmospheric water cycle changes over the xinjiang, China. J. Hydrol. 585, 124823. https://doi.org/10.1016/j.jhydrol.2020.124823.
- Yao, T., Bolch, T., Chen, D., Gao, J., Immerzeel, W., Piao, S., Su, F., Thompson, L., Wada, Y., Wang, L., Wang, T., Wu, G., Xu, B., Yang, W., Zhang, G., Zhao, P., 2022. The imbalance of the asian water tower. Nat. Rev. Earth Environ. 3, 618–632. https://doi.org/10.1038/s43017-022-00299-4.
- Yin, H., Zhang, Q., Xu, Q., Xue, W., Guo, H., Shi, Z., 2009. Characteristics of climate change in Qilian Mountains region in recent 50 years. Plateau Meteorol. 28 (01), 85–90
- Zhang, Q., Lin, J., Liu, W., Han, L., 2019. Precipitation seesaw phenomenon and its formation mechanism in the eastern and Western parts of northwest China during flood season. Sci. China Earth Sci. 49 (12), 2064–2078. https://doi.org/10.1007/s11430-018-9357-y.
- Zhang, Q., Yang, J., Wang, W., Ma, P., Lu, G., Liu, X., Yu, H., Fang, F., 2021. Climatic warming and humidification in the arid region of northwest China: multi-scale characteristics and impacts on ecological vegetation. J. Meteorol. Res. 35 (1), 113–127. https://doi.org/10.1007/s13351-021-0105-3.
- Zhang, Q., Yu, Y., Zhang, J., 2008. Characteristics of water cycle in the Qilian Mountains and the oases in hexi inland river basins. J. Glaciol. Geocryol. 30 (06), 907–913.
- Zhang, Y., Chen, F., Gou, X., Jin, L., Tian, Q., Wang, Y., Peng, J., 2007. The temporal and spatial distribution of seasonal dry-wet changes over the northwestern China: based on PDSI. Acta Geogr. Sin. 62 (11), 1142–1152.
- Zhang, Z., Wang, X., Yang, M., Liu, L., Li, J., Wang, G., 2023. Spatio-temporal changes of key climatic elements in the upper Yellow River water conservation area in recent 60 years. Plateau Meteorol. 42 (6), 1372–1385. https://doi.org/10.7522/j.issn.1000-0534.2023.00011.
- Zhao, H., Huang, W., Xie, T., Wu, X., Xie, Y., Feng, S., Chen, F., 2019. Optimization and evaluation of a monthly air temperature and precipitation gridded dataset with a 0.025° spatial resolution in China during 1951–2011. Theor. Appl. Climatol. 138 (1), 491–507. https://doi.org/10.1007/s00704-019-02830-y.
- Zhu, G., Wang, L., Liu, Y., Bhat, M.A., Qiu, D., Zhao, K., Sang, L., Lin, X., Ye, L., 2022. Snow-melt water: an important water source for picea crassifolia in Qilian Mountains. J. Hydrol. 613, 128441. https://doi.org/10.1016/j.jhydrol.2022.128441.